Characterization

Bruker AXS D8-Focus diffractometer with Cu K_α radiation (Germany) diffractometer was used to record X-ray powder diffraction (XRD) pattern. The attenuated total reflection Fourier transform infrared (ATR-FTIR) spectra of the samples were obtained with the Nicolet 6700 (Brock, America). A field emission microscope (Hitachi FESEM-4800) was used scanning electron microscope (SEM) images. Brunauer-Emmett-Teller (BET) surface areas were obtained by ASAP 2020 plus HD88 at a liquid nitrogen temperature of 77 K, and the pore size was derived from the adsorption branch of the N_2 isotherm. TGA/DSC analysis was carried out using a TA Company SDTQ600 with sample heating from room temperature to 900 °C at 10 °/min under a N_2 flow.

Adsorption tests

Each time a certain amount of DBT is weighed and dissolved in n-octane solution and configured into 1000 μg/g, 1500 μg/g and 2000 μg/g simulated oil for using. Static adsorption experiments were performed with adsorbent: simulated oil mass ratio of 1:200 and adsorbent was roasted at 423 k under N_2 atmosphere to remove water and other contaminants prior to use. The mixture was shaken at a constant temperature of 303 K for adsorption, and the supernatant was taken at regular intervals and analyzed for the amount of dibenzothiophene contained using liquid chromatography, which in turn was used to find the adsorption amount until the adsorption equilibrium point was reached. Adsorption volume calculation equation:

$$Q = \frac{m_{oil}}{m_{adsorbent}} \left(C_0 - C_e \right) \times 10^{-3} \quad (1)$$

Here, Q represents the equilibrium adsorption amount in mg/g; C_0 is the initial concentration of the simulated oil in μg/g; C_e is the concentration at equilibrium in μg/g; $m_{adsorbent}$ is the mass of the adsorbent (g); m_{oil} is the mass of the simulated oil (g).

DFT calculations

ZIF-8 is a sub-class of MOFs composed of Zn^{2+} cations coordinated via bridging imidazolate-based ligands,[1] whose precursor has the chemical formula $Zn(Meim)_2$.[2] It has a relatively large cavity (11.6 Å) and a suitable pore size (3.4 Å).[3] The initial model of the crystal was optimized by energy minimization and structure optimization with the help of density functional theory (DFT) in the generalized gradient approximation (GGA) calculation in Materials Studio. The lattice primitive unit cell (containing 12-Zn, 48-N, 95-C and 135-H atoms) parameters are $a = b = c = 16.991$, $\alpha = \beta = \gamma = 90$, which is an excellent agreement of the previous reported.[4] Its initial computational model is freely available from the Cambridge Crystallographic Data Center. And we used the Castep tool to construct a slab model of the {100} and {110} surfaces (similar to the surface endpoints of ZIF-8 proposed by Tian et al. in their experimental study). Slab were separated from their periodic images by a vacuum region of at least 20 Å in order to expose a more realistic surface for docking the DBT molecule, seen in Fig. S5.[5]

Adsorption mechanism

Nowadays, attention has been paid to the different morphologies of materials and the effect of their different crystalline surfaces on their properties. Galloway et al. [6] investigated the mechanism of sulfur oxide adsorption on {110} crystalline surfaces of CaO. Sadeghi et al. [7] investigated the interaction of the polymer with the ZIF-8 (001) and (110) surfaces through DFT simulation calculations and found that the adsorption properties may be dominated by electronic and/or electrostatic effects, possibly due to defects such as coordination unsaturated metals exist. Liu et al. [8] studied the adsorption of CTAB on different crystal planes of ZIF-8 through molecular dynamics and X-ray photoelectron spectroscopy (XPS), and found that CTAB preferentially adsorbed on the {100}, which may be because the metal atoms on the {100} have lower coordination numbers, and then controllably synthesize ZIF-8 with different crystal planes. Therefore, different facets may be the reason why the synthesized ZIF-8 materials have different adsorption performance.

In this work, we found that ZIF-8 crystals containing both {110} and {100} facets in Fig. S2. And the {110} crystallographic exposures of ZIF-8, ZIF-8 (25%), ZIF-8 (50%), and ZIF-8 (75%) were 60%, 75%, 85% and 100%, respectively, which is clearly a positive linear relationship with adsorption performance. To further validate the effect of {110} and {100} crystalline surfaces on the adsorption properties of the prepared samples, relevant model calculations were carried out. Seen in Fig. S6, the adsorption energy of a single DBT molecule adsorbed on the {100} nano-surface with a value of -27.57 eV was the lower than the energy of {110} surface with a value of -27.82 eV indicating that {110} is the most preferred one for DBT adsorption. This is in high agreement with our experimental results and ZIF-8 (75%) has the highest exposure to the {110} crystal plane and the best adsorption performance, may be resulting to the larger active area and more active sites in {110}.[9, 10]

Synthesis steps:

MAF-6: 0.745 g $Zn(NO_3)_2$ and 0.745 g $Zn(OH)_2$ was added to 75 ml ammonia to make solution A and 1.45 g 2-ethylimidazole was dissolved in 150 ml methanol and 7 ml cyclohexane solution, called solution B. After pouring solution A into solution B, the mixture was stirred for 12 h, then the mixed solution was separated and the solid was washed with methanol three times and dried to obtain MAF-6.

ZIF-71: 0.745 g $Zn(NO_3)_2$, 0.745 g $Zn(OH)_2$ and 1.20 g 4,5-dichloroimidazole was added to 50 ml methanol, separately. Then the two solutions were mixed and stirred for 12 h, and the solid was separated from the mixed solution by centrifugation, washed with methanol three times, dried and ground to obtain ZIF-71.

ZIF-11: Dissolve 2.35 g benzimidazole in 50 ml methanol as A solution, then add 20 ml toluene, and 0.745 g $Zn(NO_3)_2$, 0.745 g $Zn(OH)_2$ to A solution, mix and stir for 12 h, after centrifugation, washing and drying to obtain ZIF-11.

Table S1. Textural parameters of different ZIF samples calculated from N_2 adsorption isotherms.

Samples	S_{BET} (m^2/g)	V_t (cm^3/g)[a]	V_{micro} (cm^3/g) [a]	V_{meso} (cm^3/g) [b]	V_{micro}/V_t [a]	d_p (nm)
ZIF-8	1775	0.70	0.68	0.02	0.98	0.73
ZIF-8 (25%)	1689	1.02	0.65	0.37	0.64	0.73
ZIF-8 (50%)	1652	1.03	0.63	0.40	0.61	0.73
ZIF-8 (75%)	1571	1.02	0.60	0.42	0.59	0.73

a) Determined by nonlocal density theory (NLDFT). b) Mesopore volume calculated by subtracting the value of V_{micro} from that of V_{total}.

Table S2. Comparison of adsorption performance of the different samples.

Adsorbents	Adsorption capacity (mg/g)	References
AC	6.4	**11**
Cu-AC	10.3	**12**
Y zeolite	4.9	**13**
Ni-Cu/Al_2O_3	3.9	**14**
Ni-Ce/Al_2O_3-SiO_2	4.0	**15**
Bentonite clay	0.2	**16**
ZIF-8 (75%)	19.3	This work

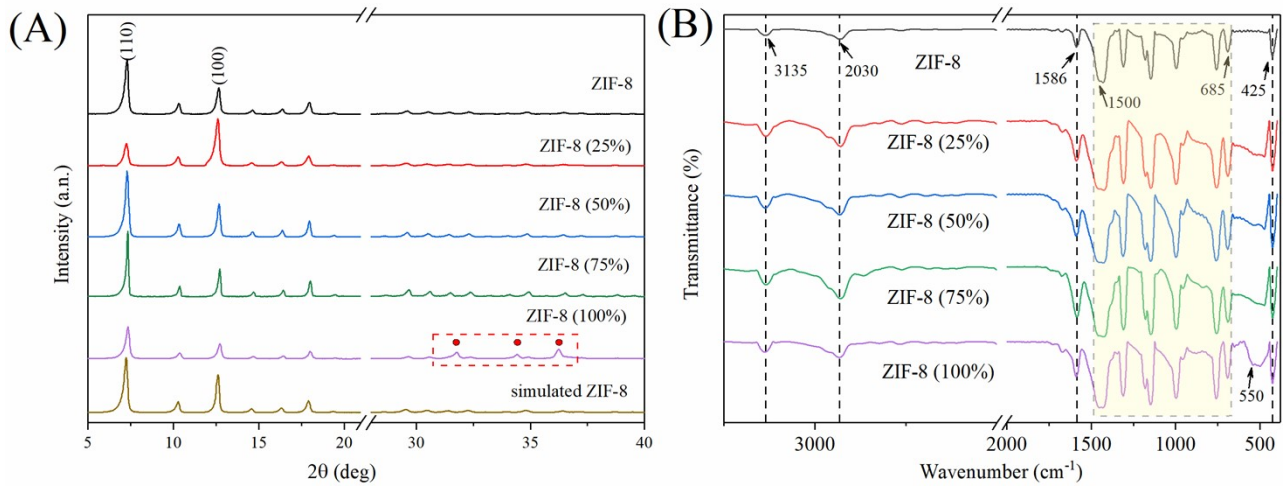

Fig. S1. (A) XRD pattern of different samples and (B) FT-IR patterns of different ZIF samples.

Fig. S1 (A) shows the XRD pattern of the different samples prepared by DZS strategy and the peak plots of the standard ZIF-8 calculated by simulation. The XRD patterns of ZIFs materials were all at 7.45°, 10.45°, 12.75°, 14.74° and 16.48° [17], corresponding to (110), (200), (110), (220) and (310) crystal planes [18], respectively. In particular, a strong sharp peak was observed at 7.45°, indicating that the material has a good crystallinity [19]. The XRD spectrum of ZIF-8 (100%) indicated the additional peaks at 31.8°, 34.9°, 36.5° and there is nothing difference exists in the range of 2θ = 5°–30°, which could be due to the unreacted $Zn(OH)_2$ residue of the starting material.

The bonding properties and purity of all sample structures were analyzed by FT-IR, as shown in Fig. S1 (B). The FT-R spectrum of the produced ZIF-8 (DZS) revealed the presence of the bands at 3135 cm^{-1} and 2030 cm^{-1} which are attributed to the aromatic and the aliphatic C-H stretch of the imidazole ring, respectively. The peak at 1586 cm^{-1} corresponds to the stretching vibration of the C=N bond and appearing at 425 cm^{-1} was assigned to the stretch mode of Zn-N. As shown in the pink dashed box in the figure, the peaks between 1500 cm^{-1} and 685 cm^{-1} are all attributed to stretching vibrations and bending vibrations of the ligand imidazole ring. And in Fig. S1 (B), the step-like transmittance peak at 550 cm^{-1} is Zn–O band [20], suggesting the existence of ZnO or $Zn(OH)_2$ in the ZIF-8 (100%), which is consistent with the XRD results. Based on the above plots shown, it can be confirmed that all samples were successfully synthesized ZIF structures.

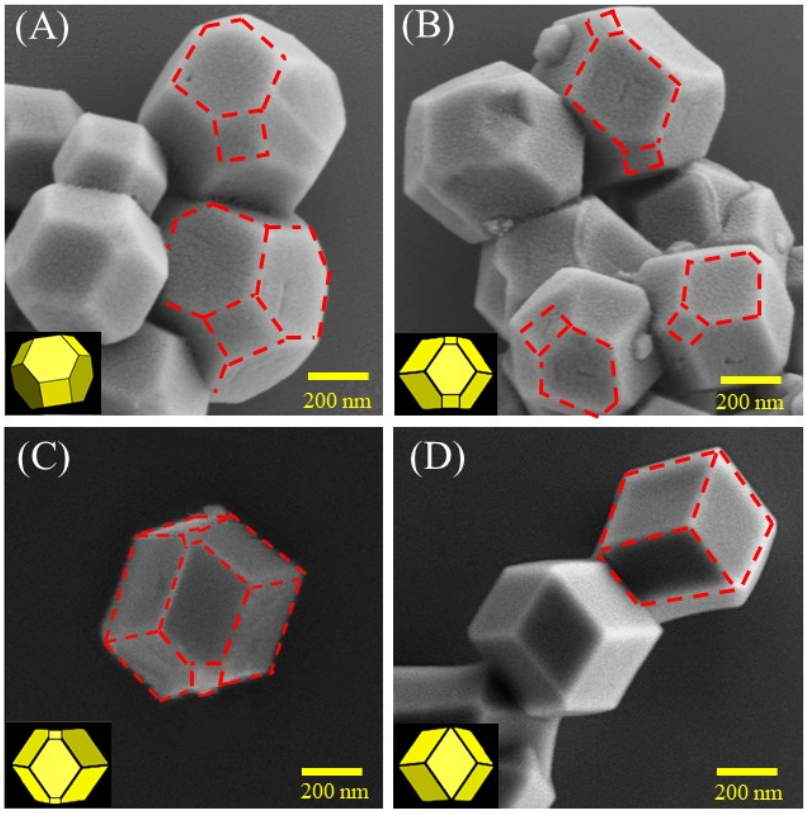

Fig. S2. SEM images of the samples: (A) ZIF-8, (B) ZIF-8 (25%), (C) ZIF-8 (50%), (D) ZIF-8 (75%) (The image inserted in the lower left corner is the model drawing made by 3ds Max.)

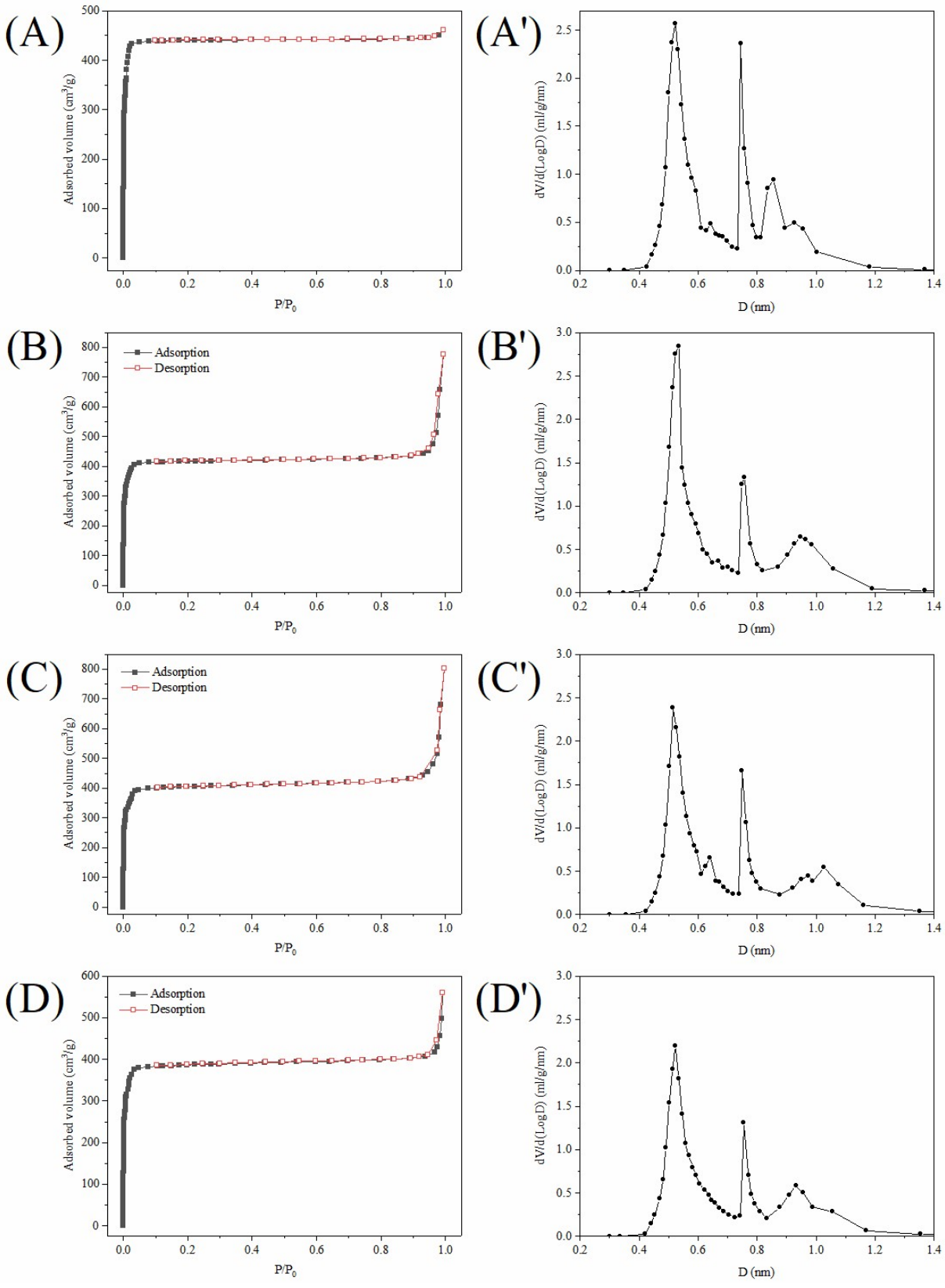

Fig. S3. The N_2 adsorption-desorption isotherm and pore size distribution curves (A, A') ZIF-8, (B, B') ZIF-8 (25%), (C, C') ZIF-8 (50%), (D, D') ZIF-8 (75%).

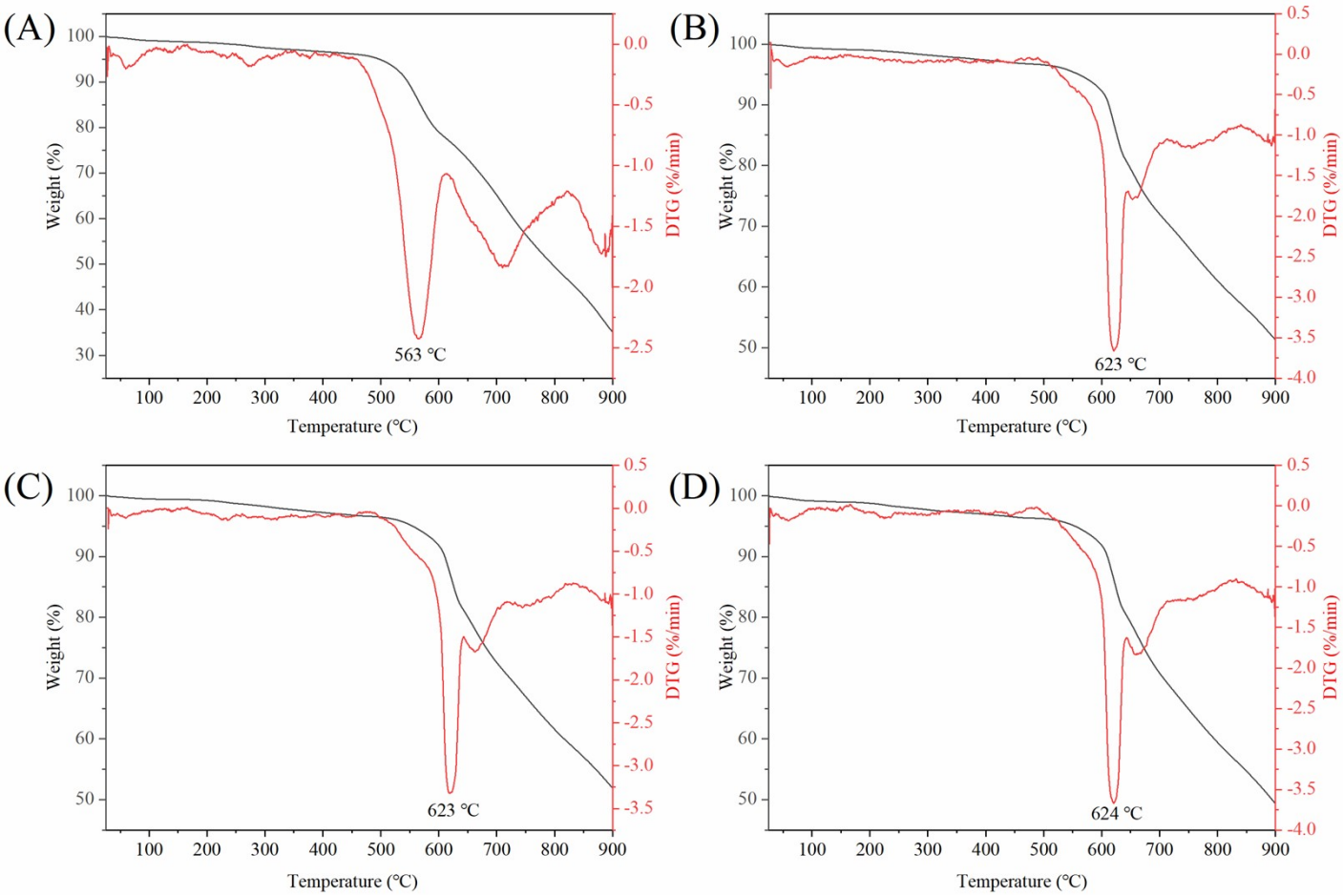

Fig. S4. Thermogravimetric curves of (A) ZIF-8, (B) ZIF-8 (25%), (C) ZIF-8 (50%), (D) ZIF-8 (75%).

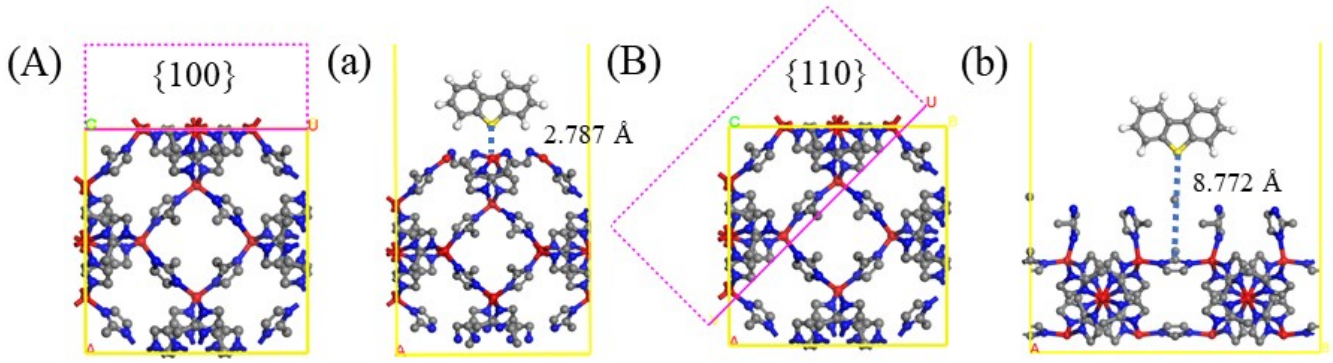

Fig. S5. ZIF-8 optimization model for different cuts face and the views of the lowest configuration of DBT molecule adsorbed on different faces. (A, a) {100} fact and (B, b) {110} fact. (The pink dashed box indicates the cutting surface, Zn are red balls and the H are hidden from view for ease of observation)

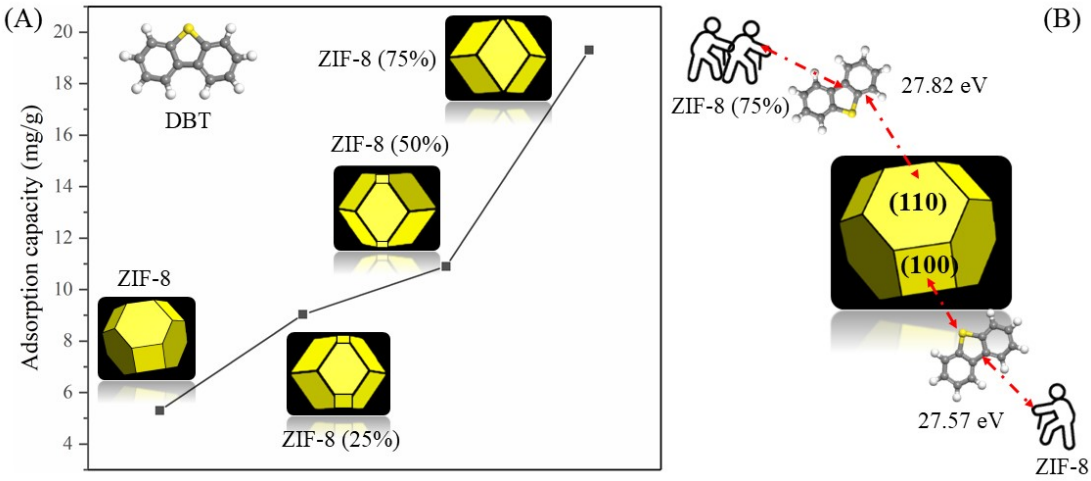

Fig. S6 (A) Relationship between the adsorption capacity of DBT by ZIF-8 with different morphologies. (B) Difference in adsorption of DBT on {110} and {100} faces.

References

1. T. Weng and J. R. Schmidt, *The Journal of Physical Chemistry C*, 2019, **124**, 1458-1468.
2. S. Shen, Y. Sun, H. Sun, Y. Pang, S. Xia, T. Chen, S. Zheng and T. Yuan, *Catalysts*, 2022, **12**, 525.
3. S. Dutta and I. S. Lee, *Materials Chemistry Frontiers*, 2021, **5**, 3986-4021.
4. M. Fischer and R. G. Bell, *CrystEngComm*, 2014, **16**, 1934-1949.
5. R. Semino, N. A. Ramsahye, A. Ghoufi and G. Maurin, *ACS Appl Mater Interfaces*, 2016, **8**, 809-819.
6. B. Galloway and B. Padak, *Fuel*, 2017, **197**, 541-550.
7. S. Sadeghi and J. D. Howe, *The Journal of Physical Chemistry C*, 2023, **127**, 3715-3725.
8. X. Y. Liu, W. S. Lo, C. Wu, B. P. Williams, L. Luo, Y. Li, L. Y. Chou, Y. Lee and C. K. Tsung, *Nano Lett.*, 2020, **20**, 1774-1780.
9. Q. Ke, Y. Duan, Y. Ji, D. Zhao, H. Zhang, C. Duan, L. Li and Y. Wei, *Journal of Chemical & Engineering Data*, 2021, **66**, 3483-3492.
10. Y. Zhu, J. Ciston, B. Zheng, X. Miao, C. Czarnik, Y. Pan, R. Sougrat, Z. Lai, C. E. Hsiung, K. Yao, I. Pinnau, M. Pan and Y. Han, *Nat Mater*, 2017, **16**, 532-536.
11. P. S. Sinhmar, A. Tiple and P. R. Gogate, *Environmental Technology & Innovation*, 2021, **22**, 101487.
12. M. Seredych and T. J. Bandosz, *Fuel Processing Technology*, 2010, **91**, 693-701.
13. A. Mansouri, A. A. Khodadadi and Y. Mortazavi, *Journal of Hazardous Materials*, 2014, **271**, 120-130.
14. G. I. Danmaliki and T. A. Saleh, *Journal of Cleaner Production*, 2016, **117**, 50-55.
15. X. Xu, S. Zhang, P. Li and Y. Shen, *Fuel*, 2013, **111**, 172-179.
16. M. C. Nilavu, B. Arunraj, H. Aggarwal and N. Rajesh, *Fuel*, 2022, **324**, 124472.
17. S. Payra, S. Challagulla, C. Chakraborty and S. Roy, *Journal of Electroanalytical Chemistry*, 2019, **853**, 113545.
18. K. Kida, M. Okita, K. Fujita, S. Tanaka and Y. Miyake, *CrystEngComm*, 2013, **15**, 1794-1801.
19. A. Gu, J. Chen, Q. Gao, M. M. Khan, P. Wang, Y. Jiao, Z. Zhang, Y. Liu and Y. Yang, *Applied Surface Science*, 2020, **516**, 146160.
20. H. Zhang, M. Zhao, Y. Yang and Y. S. Lin, *Microporous and Mesoporous Materials*, 2019, **288**, 109568.